# Interface-dominated hydroxymethanesulfonate and its isomer formation provides key mechanisms for reconciling the atmospheric sulfur budget gap in polluted and cold environments

**Yang Liu et al.**

*Correspondence to:* Ling Liu (lingliu@bit.edu.cn) and Xiuhui Zhang (zhangxiuhui@bit.edu.cn)

## Table of Contents

**Figure S4.** Convergence assessment of well-tempered metadynamics simulations for HMS and HMSi formation from HCHO and $HOSO_2^-$ reaction. Free energy profiles as a function of the collective variable (CV) at different simulation times are shown for six systems. Top row: HMS in bulk water, HMSi in bulk water, and HMSi at the air–ice interface ($T$ = 243 K). Bottom row: HMS at the air–water interface, HMSi at the air–water interface, and HMSi at the air–ice interface ($T$ = 223 K). The free energy profiles obtained at different times in the last several picoseconds do not exhibit significant variations, indicating that convergence has been achieved in all simulations.

**Figure S5.** Structural evolution of air-ice interfaces during 10 ps BOMD simulations: (a) $T$ = 243 K, featuring a quasi-liquid layer (QLL) atop crystalline ice; (b) $T$ = 223 K, showing pure crystalline ice without QLL. Structures are rendered at 500 fs intervals with a time-dependent color gradient from red (0 ps) through white to blue (10 ps).

**Figure S6.** Computational analysis of nucleophilic reactivity in $HOSO_2^-$. (a) Fukui function $f^-$ isosurface plot (green, isovalue = 0.01) and condensed Fukui function values ($f_A^-$) for potential nucleophilic sites. Sulfur and non-hydroxyl oxygen atoms exhibit significantly higher nucleophilic character ($f_A^-$ = 0.255-0.296) compared to hydroxyl oxygen O(H) ($f_A^-$ = 0.127). (b) Key structures from potential energy surface scan along the O(H)···C reaction coordinate, with interatomic distances in Å. The structural analysis confirms the absence of viable product formation via the O(H) pathway.

**Figure S7.** Free energy profiles ($\Delta G$ in kcal $mol^{-1}$) for the reactions between HCHO and $HOSO_2^-$ to form HMS and HMSi, calculated at the DLPNO-CCSD(T)/aug-cc-pVTZ//B3LYP-D3/6-311+G(d,p) level of theory. (a) HMS formation without water catalysis, (b) HMS formation with water catalysis, (c) HMSi formation without water catalysis, and (d) HMSi formation with water catalysis. Green and purple lines represent gas-phase reactions and liquid-phase reactions, respectively.

**Figure S8**. BOMD simulation snapshots of HMS formation at the air-water interface. (a) Representative structural snapshots showing the reaction progression from intermediate through transition state to product. (b) Time evolution of key bond distances during the simulation.

**Figure S9.** Electron transfer during HMS formation at the air-water interface. Time evolution of Mulliken charges on the sulfur atom of $HOSO_2^-$ and the oxygen atom of HCHO during nucleophilic addition.

**Figure S10.** Potential energy surface for the HCHO + $HOSO_2^-$ reaction at a model water interface using a $W_{10}$ cluster with $K^+$ counterion. Two pathways are shown: one leading to HMS formation and another to HMSi formation. The inset displays the intrinsic reaction coordinate profile for HMS formation. All energies are reported in kcal $mol^{-1}$, calculated at the DLPNO-CCSD(T)/aug-cc-pVTZ//B3LYP-D3/6-311+G(d,p) level.

**Figure S11.** Comparative hydrogen-bonding analysis of reactants in bulk water versus air-water interface. Stacked probability distributions indicate the number of coordinating water molecules for HCHO (left) and $HOSO_2^-$ (right).

**Figure S12.** Projected density of states (PDOS) of the key structure within the reaction of HCHO and $HOSO_2^-$ at the air-water interface (left) and in bulk water (right). The wavefunction calculations employed the PBE0 functional with triple-ζ basis sets and the Goedecker–Teter–Hutter (GTH) pseudopotentials. HOMO: highest occupied molecular orbital; LUMO: lowest unoccupied molecular orbital.

**Figure S13.** Probability distributions of the cosine of the angle θ between the OH bond vector and the z-axis (normal to the water slab interface) for (a) $HOSO_2^-$ and (b) $HCHOH^+$ at the air-water interface. The insets illustrate the definition of the angle θ and the molecular orientation relative to the z-axis.

**Figure S14.** Electrostatic potential (ESP) mapped onto the van der Waals surface of (a) formaldehyde (HCHO) and (b) protonated formaldehyde ($HCHOH^+$). The golden and cyan dots indicate the positions of ESP maxima and minima, respectively, with values given in kcal/mol. Color scale ranges from red (negative ESP) to blue (positive ESP).

**Figure S15.** Mechanistic investigation of the reaction between $HCHOH^+$ and $HSO_3^-$ in acidic environment.

**Figure S16.** Distribution of bisulfite ions ($HOSO_2^-$) in ice. (a) Snapshot structures taken from MD

simulations of the $KHOSO_2$ solution during the freezing process at $T$ = 260 K, showing the progressive exclusion of $HOSO_2^-$ ions to the ice-air interface. (b) Temporal evolution of the system's potential energy (kcal/mol) during the freezing simulation. (c) Calculated mass density (kg $m^{-3}$) of $HOSO_2^-$ ions (purple shaded region) along the Z direction, averaged over the 800-1000 ns simulation period, demonstrating the accumulation at the air-ice interface. The point (Z = 0 nm) indicates the bottom of the MD simulation box.

**Figure S17.** Projected density of states (PDOS) for the reactant complex (RC), transition state (TS), and product (P) along the HMS formation pathway from HCHO and $HOSO_2^-$ at the air-ice interface at (a) $T$ = 243 K, featuring a quasi-liquid layer atop crystalline ice, and (b) $T$ = 223 K, pure crystalline ice. The wavefunction calculations employed the PBE0 functional with triple-ζ basis sets and the Goedecker–Teter–Hutter (GTH) pseudopotentials. HOMO: highest occupied molecular orbital; LUMO: lowest unoccupied molecular orbital.

**Figure S18.** HMS formation on crystalline ice surface at $T$ = 223 K. (a) BOMD simulation snapshots showing initial configuration and reaction progression with HCHO and $HOSO_2^-$ on the ice surface. (b) Time evolution of key bond distances during the simulation.

**Figure S19.** HMSi formation at the air-quasi-liquid-layer interface ($T$ = 243 K). (a) Initial metadynamics configuration showing HCHO and $HOSO_2^-$ at the interface. (b) Free energy profile along the collective variable with a 5.38 kcal/mol barrier. Insets show reactant complex (RC), transition state (TS), and product (P) structures.

**Figure S20.** HMSi formation at the air-ice surface ($T$ = 223 K). (a) Initial metadynamics configuration showing HCHO and $HOSO_2^-$ on the crystalline ice surface. (b) Free energy profile along the collective variable with a 5.73 kcal/mol barrier. Insets show reactant complex (RC), transition state (TS), and product (P) structures.

**Figure S21.** Mechanistic investigation of the reaction between $HCHOH^+$ and $HOSO_2^-$ on ice surface.

**Figure S22.** Mechanistic investigation of the reaction between $HCHOH^+$ and $HSO_3^-$ on ice surface.

**Figure S23.** Hydration distribution (%) of (a) HMS and (b) HMSi at different relative humidity (RH = 25-100%) and temperatures ($T$ = 240-298 K).

**Figure S24.** (a) Schematic representation of the ice-air interface showing the spatial arrangement of HMS/HMSi molecules with distinct oxygen atoms labeled as Oa, Ob, Oc, and Od, where Z > 0 corresponds to the air phase and Z < 0 corresponds to the ice phase. Probability distributions of distinct oxygen atoms (Oa, Ob, Oc, and Od) as a function of distance to the ice surface for HMS (b) and HMSi (c) molecules.

## Computational Methods

## Section I. Ab Initio Molecular Dynamics Simulations

### Well-tempered Metadynamics

Metadynamics facilitates sampling by introducing an additional bias potential that acts on specific degrees of freedom, often termed collective variables (CVs)[1]. This potential is built as a sum of Gaussian kernels deposited along the trajectory in the CVs space:

$$V(s,t) = \sum_{t'=\tau_G,\tau_{2G}\cdots}^{t'<t} W \exp\left(-\sum_{i=1}^{n_s} \frac{(s_i - s_i')^2}{2\sigma_i^2}\right) \tag{S1}$$

Where $\tau_G$ is the time interval for introduction of each Gaussian, $s_i$ and $s_i'$ are the current and previous values of $s_i'$ when Gaussians were deposited, $\sigma_i$ is the width of the Gaussians in each $s_i'$, and $W$ is the height of the Gaussians.

In standard metadynamics, Gaussian kernels with fixed height are deposited throughout the simulation duration, driving the system to probe regions of elevated free energy and causing the free-energy estimate derived from the bias potential to fluctuate around its true value. In contrast, well-tempered metadynamics[2] reduces the Gaussian height progressively over time, as dictated by:

$$W = W(t') = W_0 \exp\left(-\frac{V(s',t')}{k_B \Delta T}\right) \tag{S2}$$

Here, $W_0$ denotes the initial Gaussian height, $\Delta T$ is a bias temperature which is typically a few times larger than the system temperature $T$, and $k_B$ is the Boltzmann constant. Over long times, the CVs sample an ensemble at $T+\Delta T$ exceeding the system temperature $T$. The parameter $\Delta T$ regulates free energy exploration extent: $\Delta T=0$ corresponds to conventional molecular dynamics, while $\Delta T \to \infty$ aligns with standard metadynamics. Furthermore, in well-tempered metadynamics, the bias factor is defined as the ratio of the CVs ($T + \Delta T$) to the system temperature ($T$), expressed by the following equation:

$$\gamma = \frac{T + \Delta T}{T} \tag{S3}$$

In this study, well-tempered metadynamics simulations were performed for each model over 100 ps using a bias factor of 10. Gaussian hills (width: 0.4 Å, height: 0.16 kcal/mol) were deposited every 30 fs along the collective variable defined in Figure S1. Quadratic walls restrained the sampling space, and all simulations were initiated from the reactant complex (RC) state. We evaluated free-energy barriers in different environments: bulk aqueous phase, air–water interface,

and air–ice interface. To verify convergence, we monitored the time evolution of deposited Gaussian hill heights, which should decay toward zero in well-tempered algorithms[3]. Figure S2,Figure S3 and Figure S4 confirms this convergence behavior for the HCHO and $HOSO_2^-$ reaction across all environmental conditions studied.

## Ab Initio Molecular Dynamics (AIMD) in Explicit Solvent Environments

Density functional theory (DFT) calculations employing implicit solvation models fail to capture the specific interactions between solute molecules and water molecules. Therefore, ab initio molecular dynamics (AIMD) simulations augmented by metadynamics-biased method were employed to study the reaction between HCHO and $HOSO_2^-$ in aqueous solution. The bulk solution environment was modeled using 128 water molecules contained within a cubic simulation box with dimensions of 1.7 nm × 1.7 nm × 1.7 nm (x × y × z). All AIMD simulations simulation parameters were identical to those detailed in the Methods section of the main text.

To simulate interfacial reactions, we extended the aforementioned bulk model by elongating the z-dimension of the simulation box to 4.7 nm while maintaining the same number of water molecules (128) and xy-dimensions (1.7 nm × 1.7 nm), thereby creating vacuum layers above and below the water slab and forming two air–water interfaces.

Potassium ($K^+$) counterion was used in all AIMD simulations to neutralize the negative charge of the bisulfite species, thereby maintaining overall system electroneutrality.

## Ice surface modeling

Ice covers approximately 10% of Earth's surface, serving as a key catalyst for atmospheric chemical reactions due to its unique properties[4].

To investigate interfacial phenomena at subfreezing conditions, we constructed an air-quasi-liquid layer model at 243 K using Born–Oppenheimer molecular dynamics (BOMD) simulations. The ice structure was derived from the hexagonal ice ($I_h$) unit cell parameters reported by Hayward et al. [5], with periodic boundary conditions applied in all three dimensions. Based on this well-built ice layer, we retained 72 water molecules in a crystalline arrangement and positioned 24 additional $H_2O$ molecules in a disordered configuration above the surface using Packmol[6], thereby forming the quasi-liquid layer (QLL). Subsequently, we extended the vacuum layer above the QLL to represent the air phase, utilizing a simulation cell of 13.52 Å × 15.61 Å × 30.00 Å (x × y × z). Prior to the pre-equilibration, the studied system undergoes full relaxation by the structural optimization.

Subsequently, a sufficient 10-ps pre-equilibration was performed using BOMD molecular dynamics.

Figure S5a illustrates the structural evolution of the air-ice interface during the pre-equilibration process. The lower ice layer effectively maintains the hexagonal crystalline structure characteristic of ice, while the upper water molecules exhibit disordered motion. This interface configuration demonstrates the successful implementation of our phase coexistence model, with proper maintenance of the crystalline ice structure at the bottom and appropriate representation of liquid water dynamics at the top. In addition to the QLL-containing system, we investigated the pure air-ice interface at $T$ = 223 K without a QLL layer, as demonstrated in previous studies[7] (Figure S5b). This panel displays the structural evolution during the 10 ps trajectory at this lower temperature, where the interface maintains a purely crystalline character. The surface propensity of $HOSO_2^-$ ions at ice interfaces was investigated using classical molecular dynamics simulations, as described in Section III. Additional computational parameters for the BOMD simulations are detailed in the Methods section of the main text.

## Density profile of interfacial water

The air-water interface was characterized through density profiles obtained from molecular dynamics slab simulations. Density distributions along the surface normal (z-axis) were calculated and fit to a hyperbolic tangent function[8]:

$$\rho(z) = \frac{1}{2}(\rho_l + \rho_v) - \frac{1}{2}(\rho_l - \rho_v)\tanh\left(\frac{z - z_{GDS}}{\delta}\right) \quad \text{(S4)}$$

where $\rho_l$ represents the density of bulk water, and $\rho_v$ is the density of the water vapor phase. The $\rho_v$ value was set to zero during the density profile fitting. In Eq. (S4), $Z_{GDS}$ is the z-coordinate of the Gibbs dividing surface (the point where the density is half of the bulk water density), and $\delta$ is the thickness parameter of the interface. And the thickness of air-water interface has been defined as $Z_{GDS} - 2\delta < Z < Z_{GDS} + 2\delta$.

## Section II. Density Functional Theory Calculations

### Multi-step conformation search

To investigate the hydrophilicity of hydroxymethane sulfonate (HMS) and hydroxymethyl sulfite (HMSi), we performed a systematic multi-step conformational search to characterize their gas-phase hydrated complexes. The artificial bee colony algorithm combined with the UFF force field generated 5000 configurations for each cluster using ABCluster[9-10]. From these, 1000 relatively stable structures were selected and pre-optimized at the PM7 level using MOPAC 2016[11-12]. The lowest-energy 100 structures were then re-optimized at the B3LYP-D3/6-31+G* level[13]. Finally, the 10 lowest-energy isomers were refined at the B3LYP-D3/6-311+G(d,p) level to identify the global minimum structure[14].

### Hydration distribution

We calculated the hydration distribution of the these components based on the following Eq. (S5):

$$f(\mathrm{CW}_i) = \frac{[\mathrm{CW}_i]}{\sum_{j=0}^{jmax} [\mathrm{CW}_i]} \tag{S5}$$

where C is a dry molecule or cluster other than water, W is water, $CW_i$ is the cluster consisting of C and $i$ water molecules, and $[CW_i]$ is the concentration of cluster $CW_i$.

$$\frac{[\mathrm{CW}_i]}{[\mathrm{C}]} = \left(\frac{[\mathrm{W}]\, k_B T}{p_{\mathrm{ref}}}\right)^i \exp\left(\frac{\Delta G(\mathrm{C}) - \Delta G(\mathrm{CW}_i)}{k_B T}\right) \tag{S6}$$

where [W] is the concentration of water vapor and $p_{\mathrm{ref}}$ is the reference pressure (in this case 1 atm) in which the Gibbs free energies are calculated as Eq. (S7):

$$\Delta G = \Delta E_{\mathrm{DLPNO-CCSD(T)}} + \Delta G_{\mathrm{thermal}}^{\mathrm{B3LYP-D3}} \tag{S7}$$

where $\Delta E_{\mathrm{DLPNO–CCSD(T)}}$ is the electronic contribution calculated at the DLPNO–CCSD(T)/aug-cc-pVTZ level of theory, and $\Delta G_{\mathrm{thermal}}^{\mathrm{B3LYP-D3}}$ is the thermal contribution calculated at the B3LYP-D3/6-311+G(d,p) level of theory. Here, we have calculated (Figure S23) relative hydrate population (%) of the $(X)_1(H_2O)_n$ clusters (X = HMS or HMSi ; $n$ = 0 ~ 3) at different relative humidity (RH = 25%, 50%,75%, and 100%) and and temperatures ($T$ = 240-298 K).

### Wave function analysis

All wave function analysis was performed using Multiwfn 3.8 (dev) code[15]. Fukui function analysis evaluated the nucleophilic reactivity of atoms within the $HOSO_2^-$ anion, which contains

two types of oxygen atoms: hydroxyl oxygen O(H) and non-hydroxyl oxygen atoms. Isosurface plots and condensed Fukui function values (Figure S6) reveal nucleophilic reactivity in the order S (0.296) > O (0.255) > O(H) (0.127), indicating that sulfur exhibits the highest nucleophilicity, followed by non-hydroxyl oxygen atoms, while hydroxyl oxygen displays the lowest reactivity. Electron density difference maps were analyzed to reveal charge transfer between reactant fragments. To identify the vacant sites of the interfacial reactants HCHO and $HCHOH^+$, we performed an electrostatic potential (ESP) analysis, as shown in Figure S13.

## Energy decomposition analysis (sobEDAw)

We performed energy decomposition analysis using the sobEDAw method to elucidate the driving forces governing reactant approach during the HCHO + $HOSO_2^-$ interfacial reaction. This analysis provides quantitative insights into how various intermolecular interactions evolve throughout the reaction process, enabling a deeper understanding of the underlying reaction mechanism (Figure 4). We reduced computational costs by employing a 10-water cluster ($W_{10}$) model that maintains chemical accuracy while representing the minimal water interface. Previous studies validated this approach[16]. The $W_{10}$ coordinates were obtained from the work of Pérez and coworkers[17]. We validated this model by investigating HMS and HMSi formation on the $W_{10}$ surface. We employed $K^+$ as the counterion to ensure both charge neutrality and consistency with our BOMD simulations. As shown in Figure S10, calculations at the DLPNO-CCSD(T)/aug-cc-pVTZ//B3LYP-D3/6-311+G(d,p) level of theory demonstrated that this model successfully reproduces the key features observed in our BOMD simulations, confirming its suitability for mechanistic analysis. These findings validated the $W_{10}$ model as an appropriate system for investigating energy decomposition along the reaction pathway.

The sobEDAw method is an advanced energy decomposition approach designed specifically for analyzing weak intermolecular interactions[18]. This method provides dispersion-to-electrostatic ratios that accurately reproduce high-level symmetry-adapted perturbation theory (SAPT) results while maintaining the computational efficiency of density functional theory. The approach decomposes total interaction energies into four physically interpretable components as follows:

$$\Delta E_{\mathrm{int}} = \Delta E_{\mathrm{els}} + \Delta E_{\mathrm{xrep}} + \Delta E_{\mathrm{orb}} + \Delta E_{\mathrm{disp}} \tag{S8}$$

where $\Delta E_{\mathrm{els}}$ represents electrostatic interactions, $\Delta E_{\mathrm{xrep}}$ denotes exchange-repulsion effects, $\Delta E_{\mathrm{orb}}$ accounts for orbital relaxation and charge-transfer contributions, and $\Delta E_{\mathrm{disp}}$ denotes dispersion

interactions. For the sobEDAw analysis, we employed B3LYP-D3/6-311+G(2d,p) w.CB (with complex basis functions in monomer calculations), which reliably reproduces CCSD(T)/CBS-quality results at significantly reduced computational cost[18].

## Section III. Classical MD Simulations

To investigate the feasibility of HMS and HMSi formation at ice surfaces, we performed classical molecular dynamics simulations to examine the distribution of $HOSO_2^-$ ions in frozen salt solutions, specifically investigating whether these ions preferentially migrate to the ice surface. The simulation model was constructed following the approach described by Ning et al[19]. Water molecules were represented using the TIP4P/ICE model[20], which accurately reproduces the properties of ice phases, while the OPLS-AA force field[21] was applied to describe all ionic species ($K^+$ and $HOSO_2^-$). This scheme has been demonstrated to be feasible[7]. All simulations employed the canonical (NVT) ensemble at 260 K with velocity-rescaling thermostat temperature control. This temperature, which is below the melting point of the TIP4P/ICE model (~273 K)[22], has been shown in multiple previous studies to allow for reliable observation of ice formation phenomena[22-23]. A timestep of 1 fs was used to integrate the equations of motion over a total simulation time of 1000 ns, providing adequate sampling of the ion distribution. Non-bonded interactions were described using standard Lennard-Jones and Coulomb potentials. The particle-mesh Ewald summation method was used to calculate electrostatic interactions[24]. All MD simulations were performed using the GROMACS package[25].

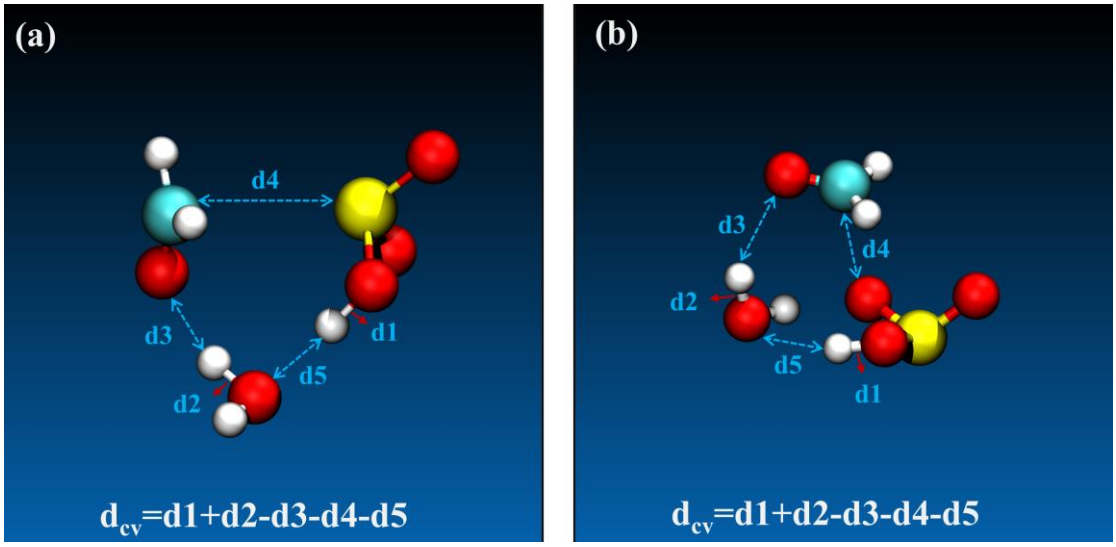


**Figure S1.** The collective variable (CV) defined for the metadynamics-biased BOMD simulation of (a) HMS and (b) HMSi

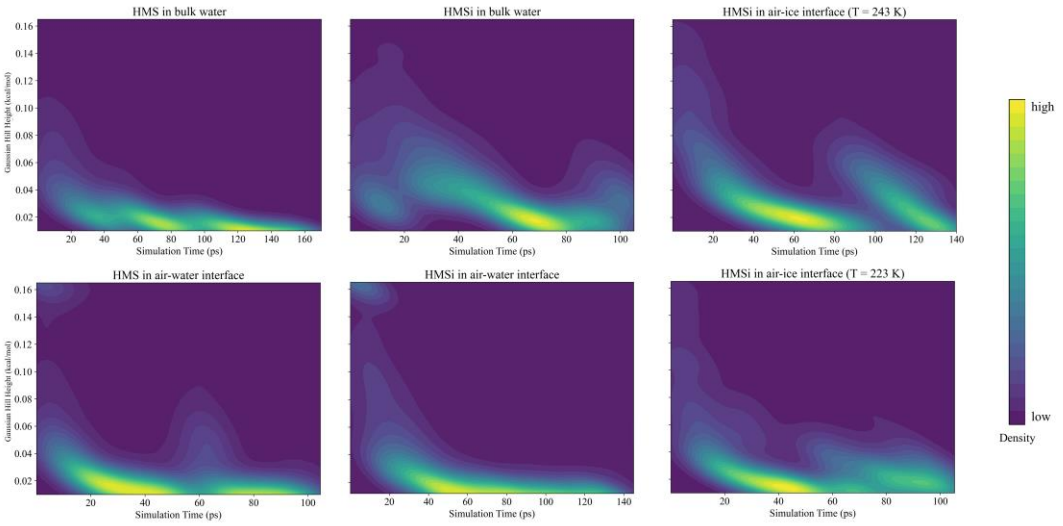


**Figure S2.** Time evolution of Gaussian hill heights (kcal/mol) from well-tempered metadynamics simulations for HMS and HMSi formation from HCHO and $HOSO_2^-$ reaction. Top row: HMS in bulk water, HMSi in bulk water, and HMSi at air-ice interface ($T$ = 243 K). Bottom row: HMS at air-water interface, HMSi at air-water interface, and HMSi at air-ice interface ($T$ = 223 K). Color gradient indicates density distribution from low (purple) to high (yellow).

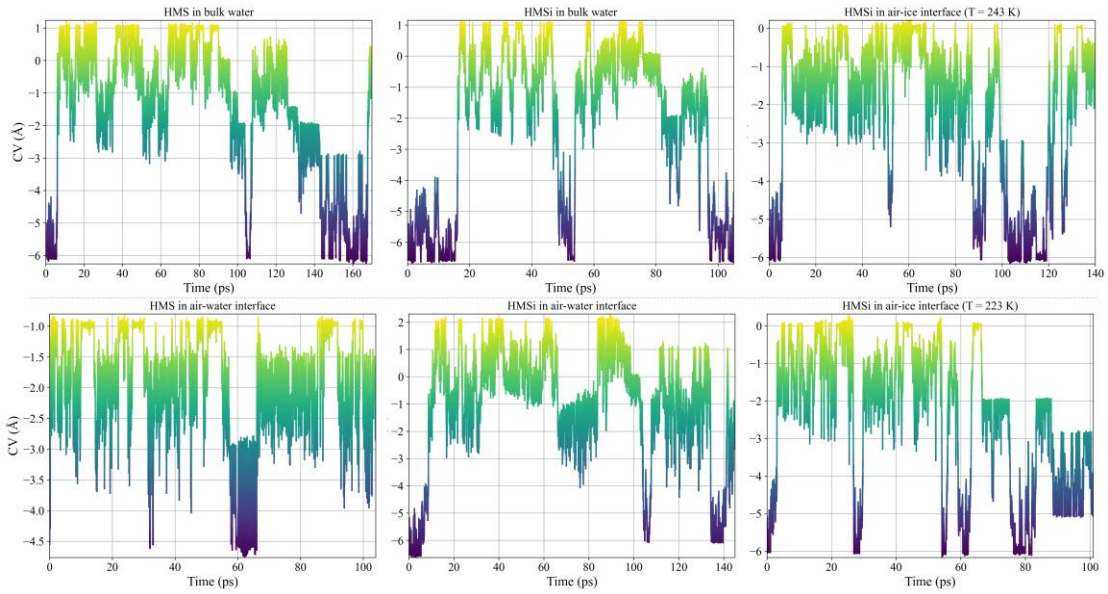


**Figure S3.** Time evolution of collective variables (CV, Å) during well-tempered metadynamics simulations for HMS and HMSi formation from HCHO and $HOSO_2^-$ reaction. Top row: HMS in bulk water, HMSi in bulk water, and HMSi at air-ice interface ($T$ = 243 K). Bottom row: HMS at air-water interface, HMSi at air-water interface, and HMSi at air-ice interface ($T$ = 223 K). Color gradient represents CV values from high (yellow-green) to low (purple).

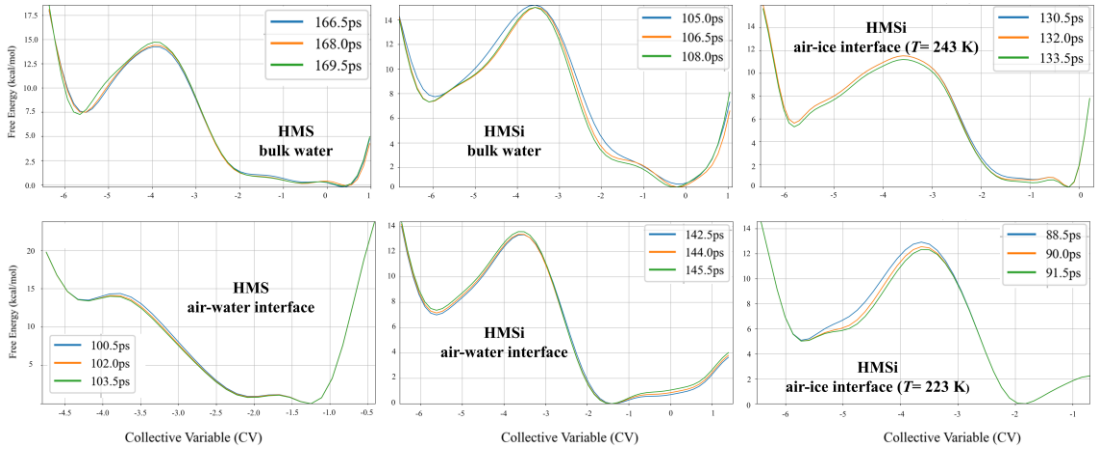


**Figure S4.** Convergence assessment of well-tempered metadynamics simulations for HMS and HMSi formation from HCHO and $HOSO_2^-$ reaction. Free energy profiles as a function of the collective variable (CV) at different simulation times are shown for six systems. Top row: HMS in bulk water, HMSi in bulk water, and HMSi at the air–ice interface ($T$ = 243 K). Bottom row: HMS at the air–water interface, HMSi at the air–water interface, and HMSi at the air–ice interface ($T$ = 223 K). The free energy profiles obtained at different times in the last several picoseconds do not exhibit significant variations, indicating that convergence has been achieved in all simulations.

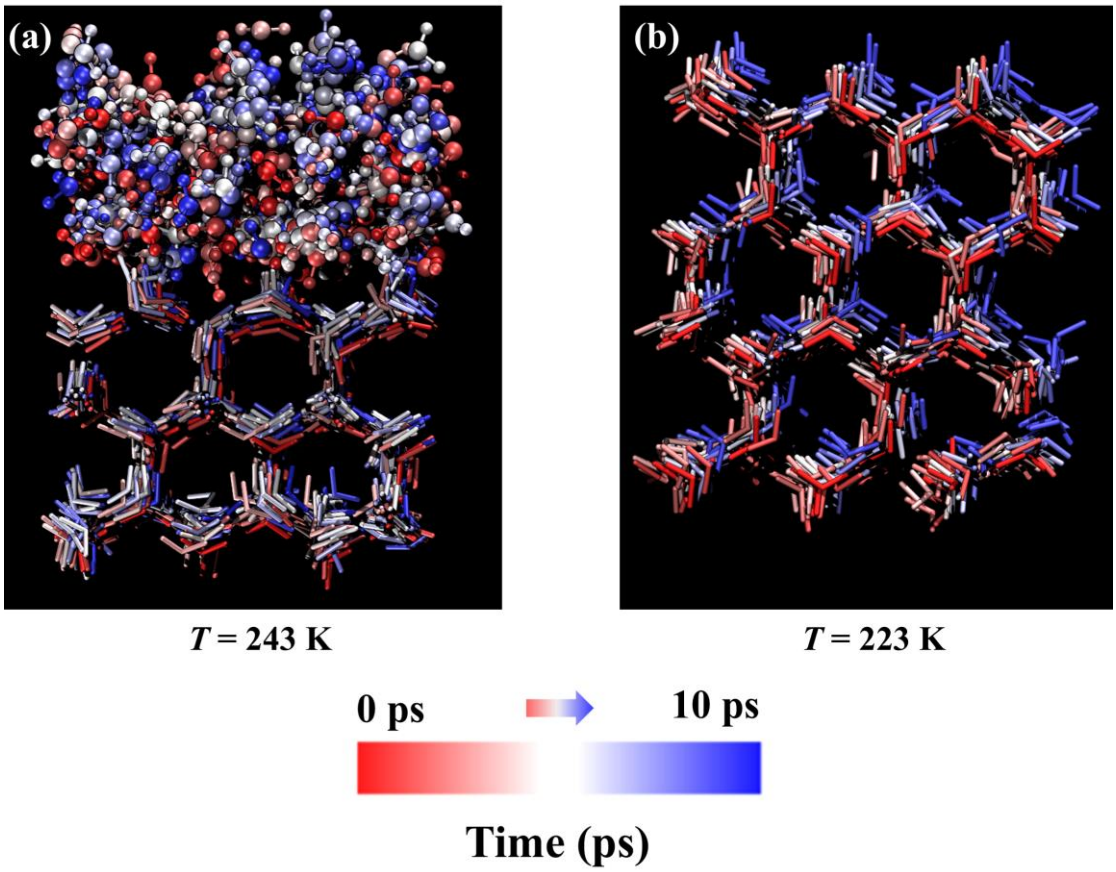


**Figure S5.** Structural evolution of air-ice interfaces during 10 ps BOMD simulations: (a) $T$ = 243 K, featuring a quasi-liquid layer (QLL) atop crystalline ice; (b) $T$ = 223 K, showing pure crystalline ice without QLL. Structures are rendered at 500 fs intervals with a time-dependent color gradient from red (0 ps) through white to blue (10 ps).

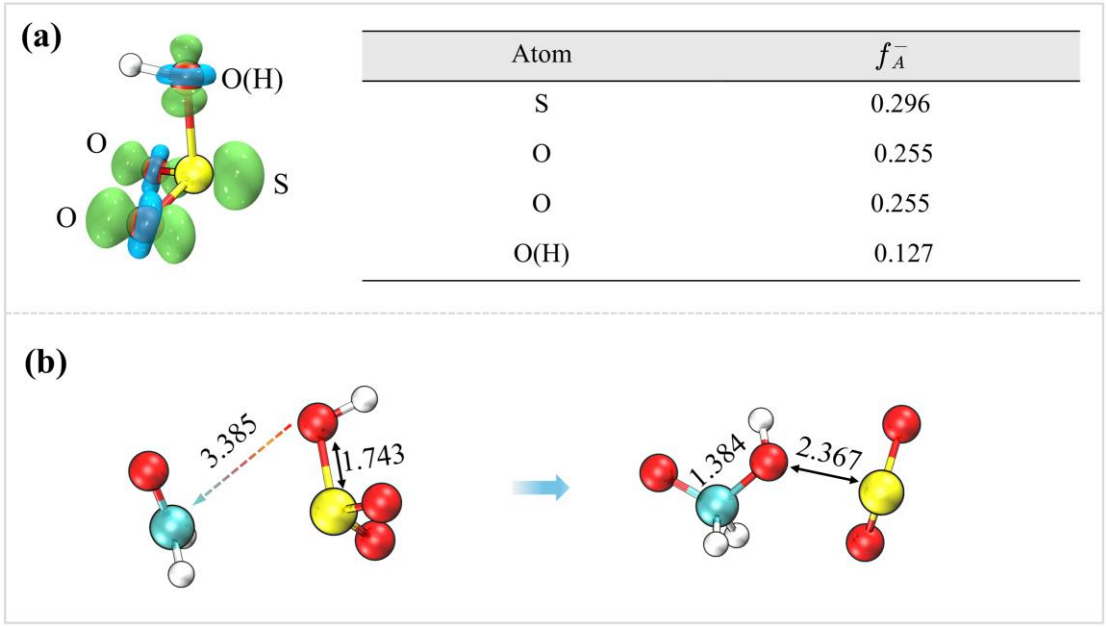


| Atom | $f_A^-$ |
|---|---|
| S | 0.296 |
| O | 0.255 |
| O | 0.255 |
| O(H) | 0.127 |

**Figure S6.** Computational analysis of nucleophilic reactivity in $HOSO_2^-$. (a) Fukui function $f^-$ isosurface plot (green, isovalue = 0.01) and condensed Fukui function values ($f_A^-$) for potential nucleophilic sites. Sulfur and non-hydroxyl oxygen atoms exhibit significantly higher nucleophilic character ($f_A^-$ = 0.255-0.296) compared to hydroxyl oxygen O(H) ($f_A^-$ = 0.127). (b) Key structures from potential energy surface scan along the O(H)···C reaction coordinate, with interatomic distances in Å. The structural analysis confirms the absence of viable product formation via the O(H) pathway.

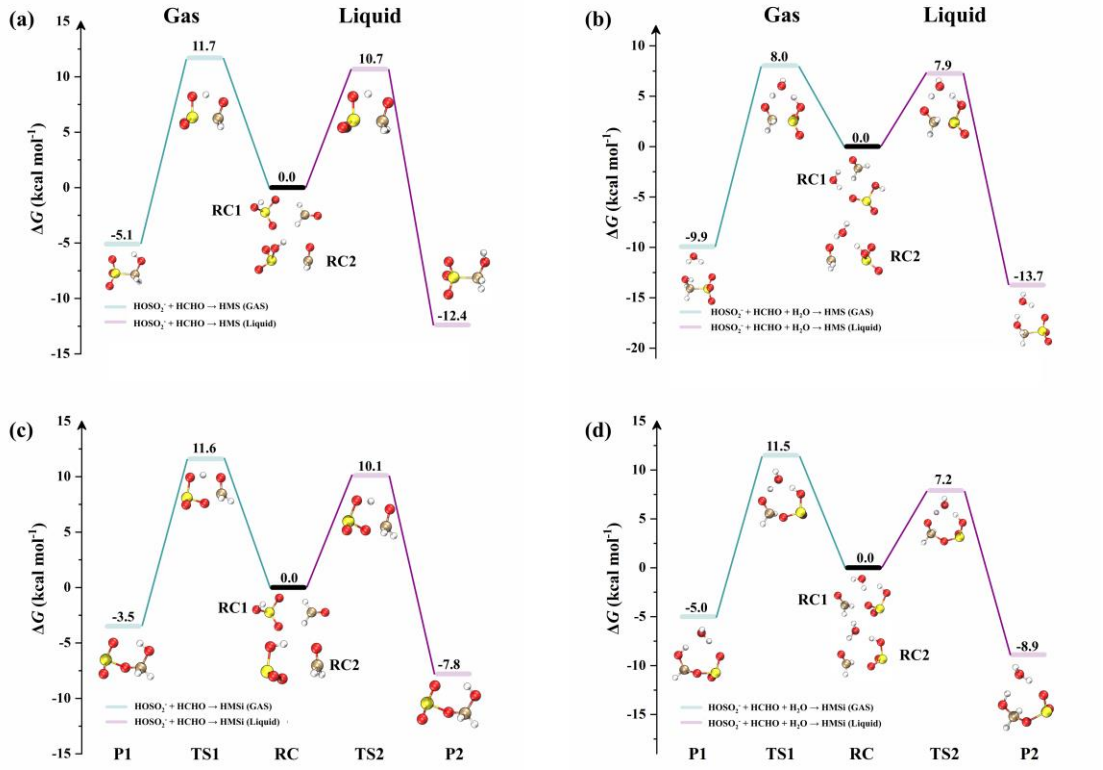


**Figure S7.** Free energy profiles ($\Delta G$ in kcal mol$^{-1}$) for the reactions between HCHO and $HOSO_2^-$ to form HMS and HMSi, calculated at the DLPNO-CCSD(T)/aug-cc-pVTZ//B3LYP-D3/6-311+G(d,p) level of theory. (a) HMS formation without water catalysis, (b) HMS formation with water catalysis, (c) HMSi formation without water catalysis, and (d) HMSi formation with water catalysis. Green and purple lines represent gas-phase reactions and liquid-phase reactions, respectively.

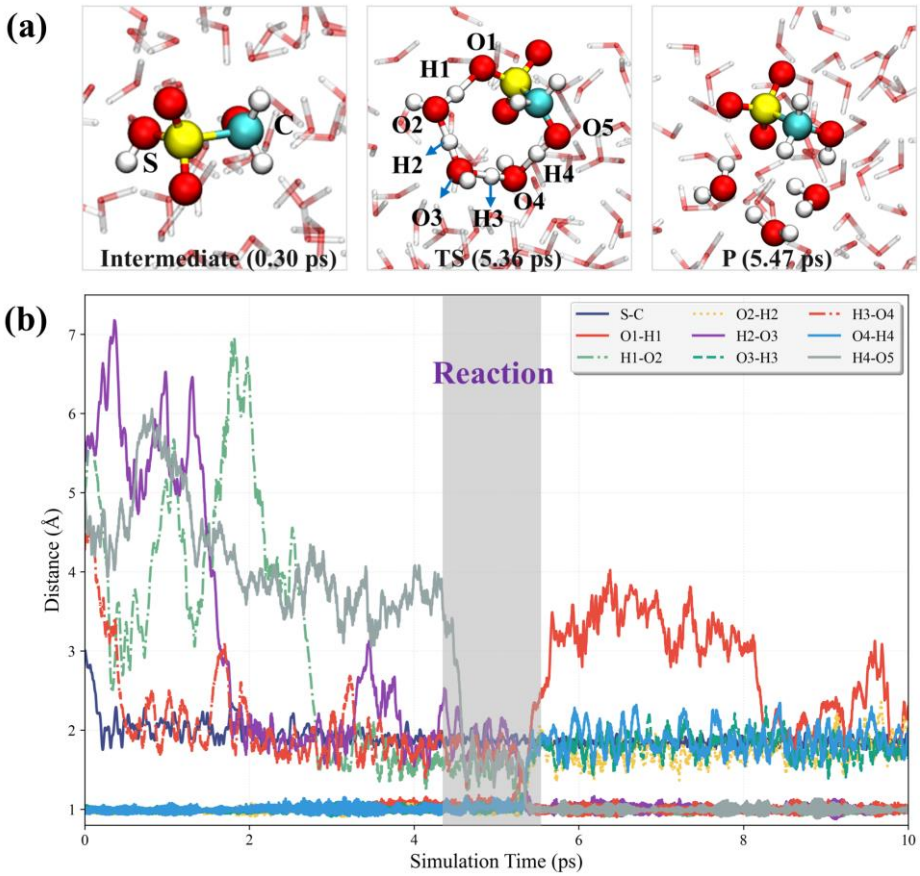


**Figure S8**. BOMD simulation snapshots of HMS formation at the air-water interface. (a) Representative structural snapshots showing the reaction progression from intermediate through transition state to product. (b) Time evolution of key bond distances during the simulation.

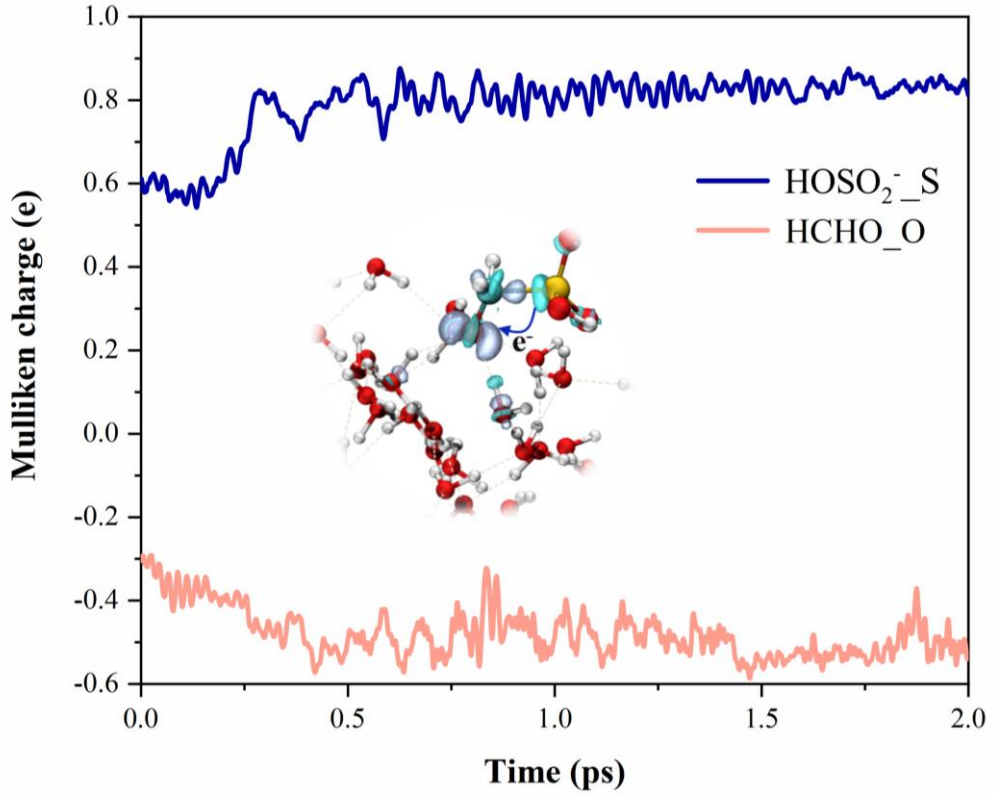


**Figure S9.** Electron transfer during HMS formation at the air-water interface. Time evolution of Mulliken charges on the sulfur atom of $HOSO_2^-$ and the oxygen atom of HCHO during nucleophilic addition.

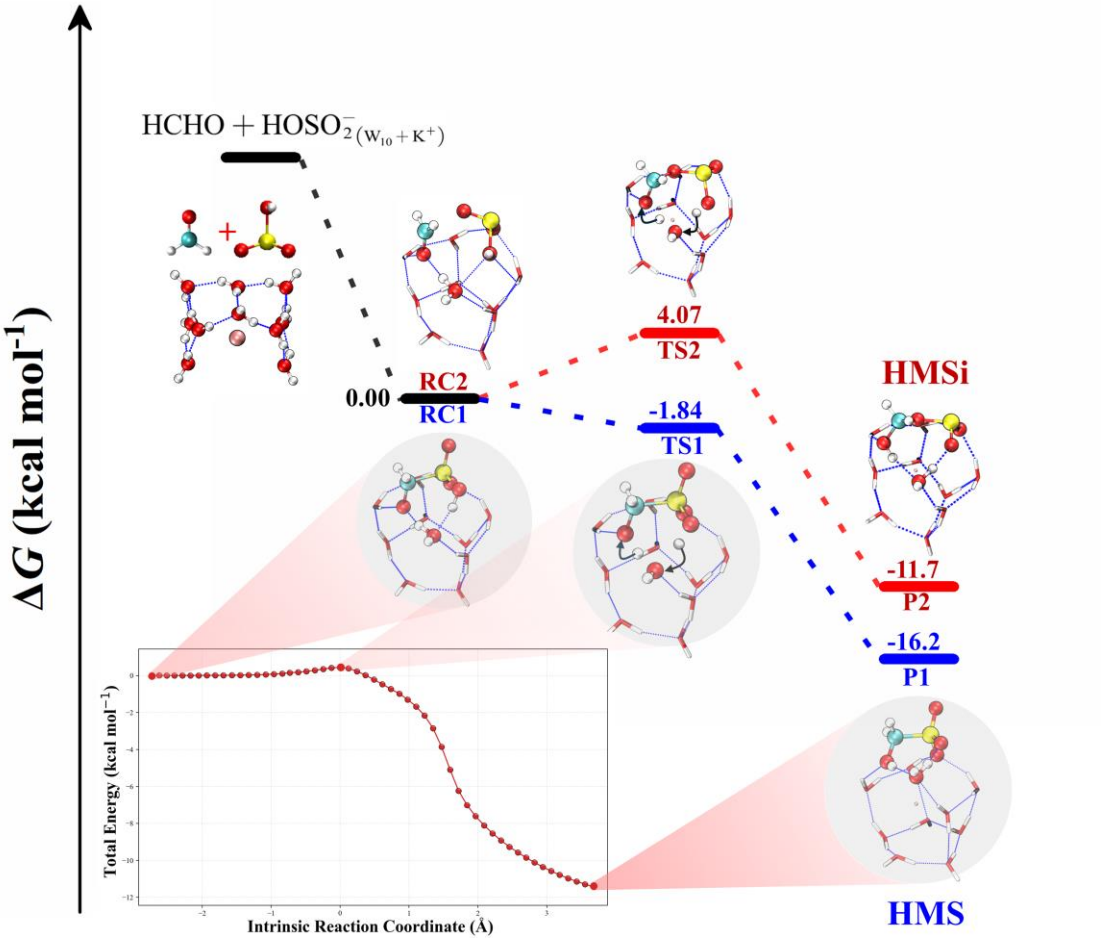


**Figure S10.** Potential energy surface for the HCHO + $HOSO_2^-$ reaction at a model water interface using a $W_{10}$ cluster with $K^+$ counterion. Two pathways are shown: one leading to HMS formation and another to HMSi formation. The inset displays the intrinsic reaction coordinate profile for HMS formation. All energies are reported in kcal $mol^{-1}$, calculated at the DLPNO-CCSD(T)/aug-cc-pVTZ//B3LYP-D3/6-311+G(d,p) level.

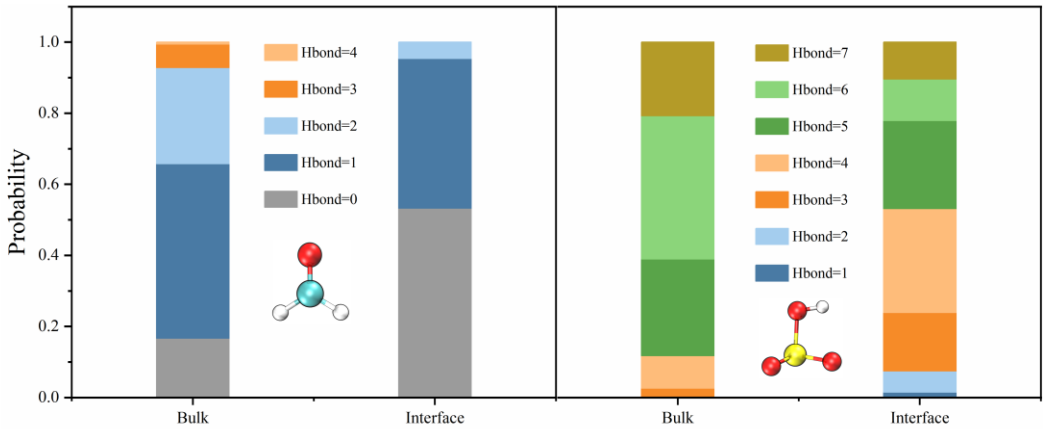


**Figure S11.** Comparative hydrogen-bonding analysis of reactants in bulk water versus air-water interface. Stacked probability distributions show the total number of hydrogen bonds formed between a single reactant molecule (HCHO, left; $HOSO_2^-$, right) and surrounding water molecules.

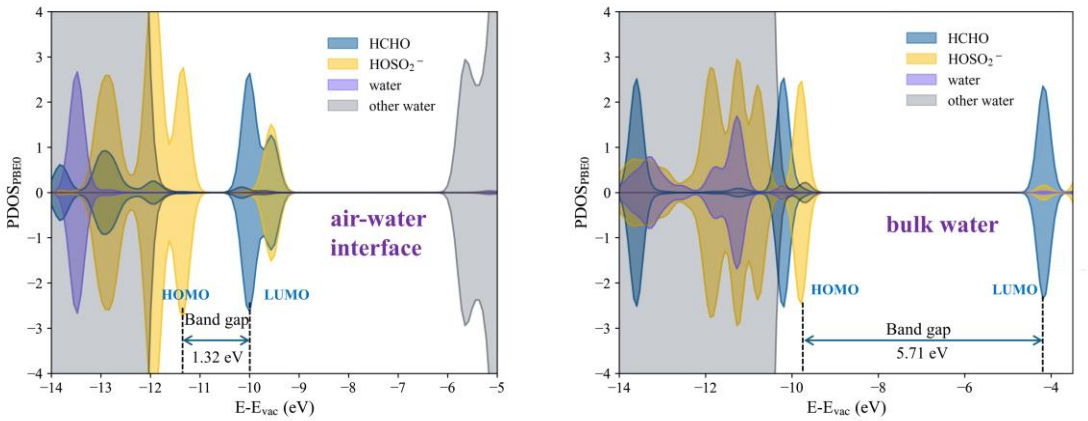


**Figure S12.** Projected density of states (PDOS) of the key structure within the reaction of HCHO and $HOSO_2^-$ at the air-water interface (left) and in bulk water (right). The wavefunction calculations employed the PBE0 functional with triple-ζ basis sets and the Goedecker–Teter–Hutter (GTH) pseudopotentials. HOMO: highest occupied molecular orbital; LUMO: lowest unoccupied molecular orbital.

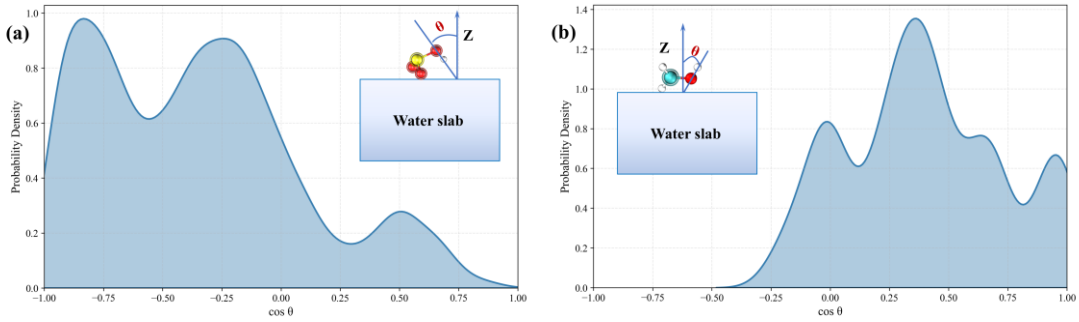


**Figure S13.** Probability distributions of the cosine of the angle θ between the OH bond vector and the z-axis (normal to the water slab interface) for (a) $HOSO_2^-$ and (b) $HCHOH^+$ at the air-water interface. The insets illustrate the definition of the angle θ and the molecular orientation relative to the z-axis.

**Related discussions**

The angular distributions in Figure S13 show that the ratio of integrated areas for cos θ > 0 to cos θ < 0 is 4:1 for $HOSO_2^-$ and 1:4 for $HCHOH^+$. Accordingly, the 25 independent BOMD trajectories were initialized following these statistical weights: ~80% of $HOSO_2^-$ orientations with cos θ > 0 and ~20% with cos θ < 0, whereas the opposite distribution (~20% with cos θ > 0 and ~80% with cos θ < 0) was applied for $HCHOH^+$. This sampling strategy ensures representative coverage of all four possible orientation combinations weighted by their interfacial occurrence probabilities.

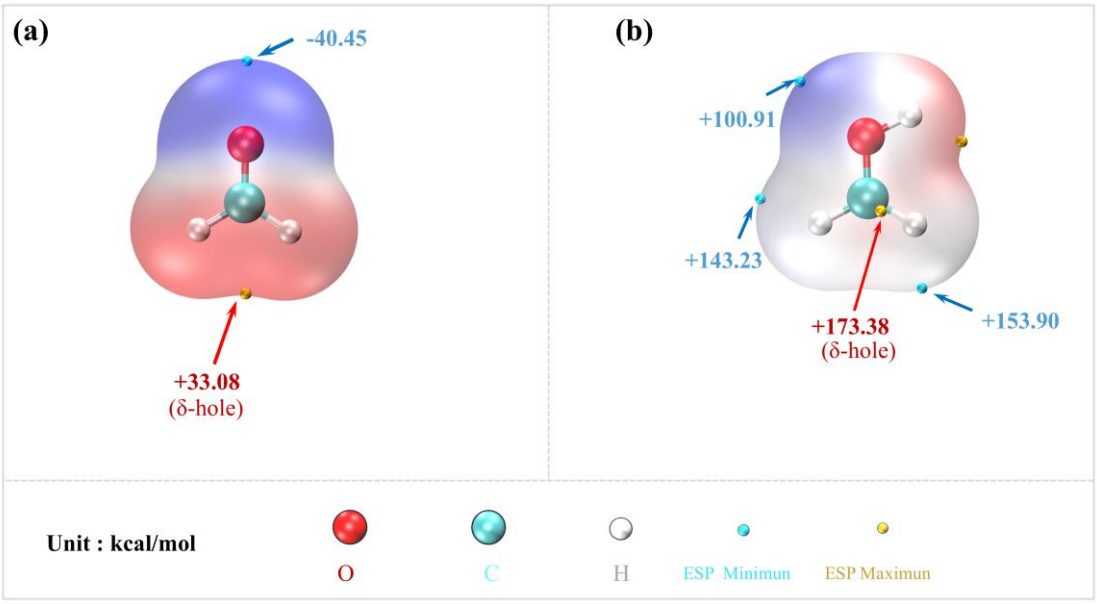


**Figure S14.** Electrostatic potential (ESP) mapped onto the van der Waals surface of (a) formaldehyde (HCHO) and (b) protonated formaldehyde ($HCHOH^+$). The golden and cyan dots indicate the positions of ESP maxima and minima, respectively, with values given in kcal/mol. Color scale ranges from red (negative ESP) to blue (positive ESP).

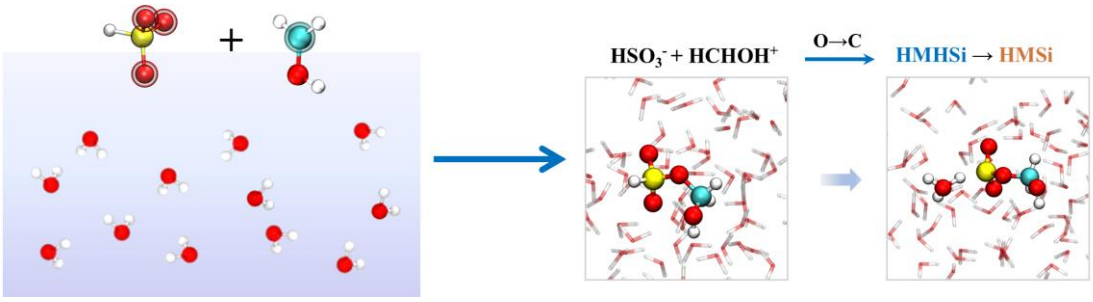


**Figure S15.** Mechanistic investigation of the reaction between $HCHOH^+$ and $HSO_3^-$ in acidic environment.

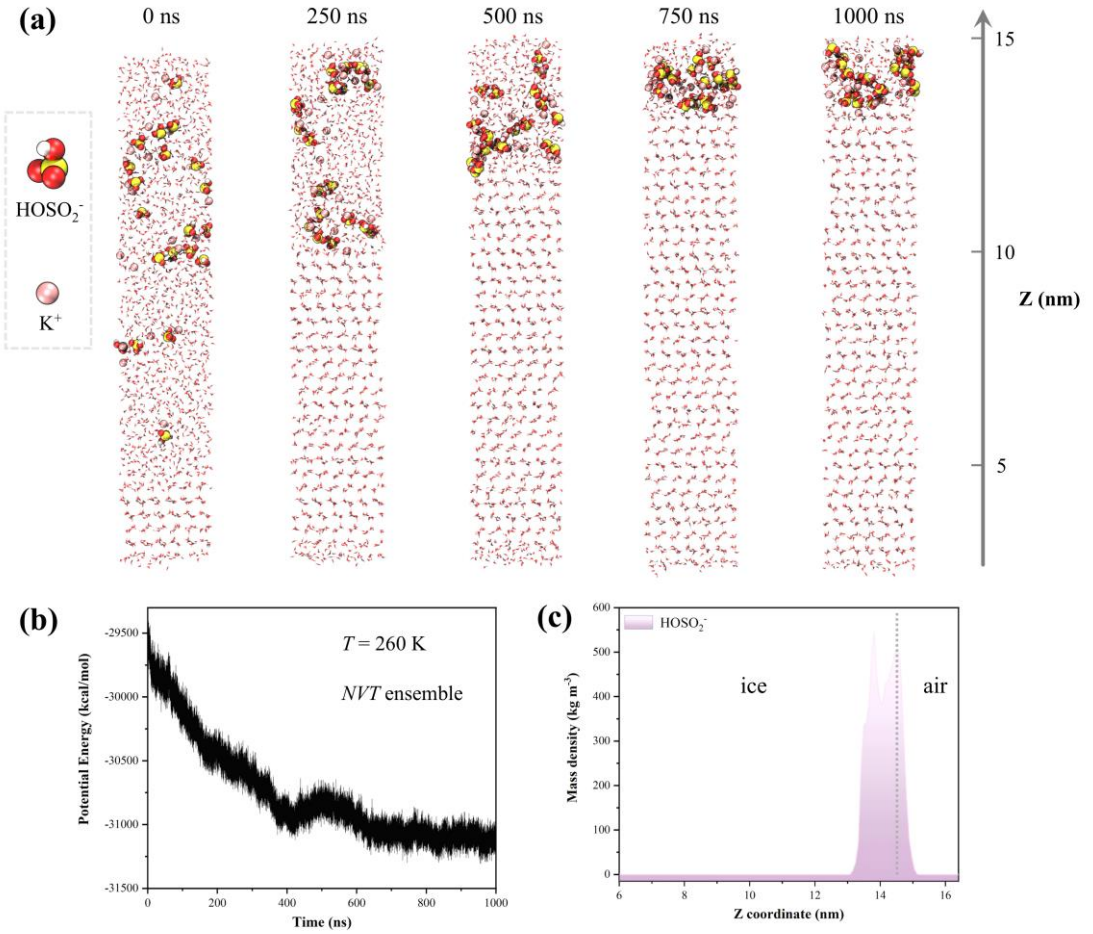


**Figure S16.** Distribution of bisulfite ions ($HOSO_2^-$) in ice. (a) Snapshot structures taken from MD simulations of the $KHOSO_2$ solution during the freezing process at $T$ = 260 K, showing the progressive exclusion of $HOSO_2^-$ ions to the ice-air interface. (b) Temporal evolution of the system's potential energy (kcal/mol) during the freezing simulation. (c) Calculated mass density (kg $m^{-3}$) of $HOSO_2^-$ ions (purple shaded region) along the Z direction, averaged over the 800-1000 ns simulation period, demonstrating the accumulation at the air-ice interface. The point (Z = 0 nm) indicates the bottom of the MD simulation box.

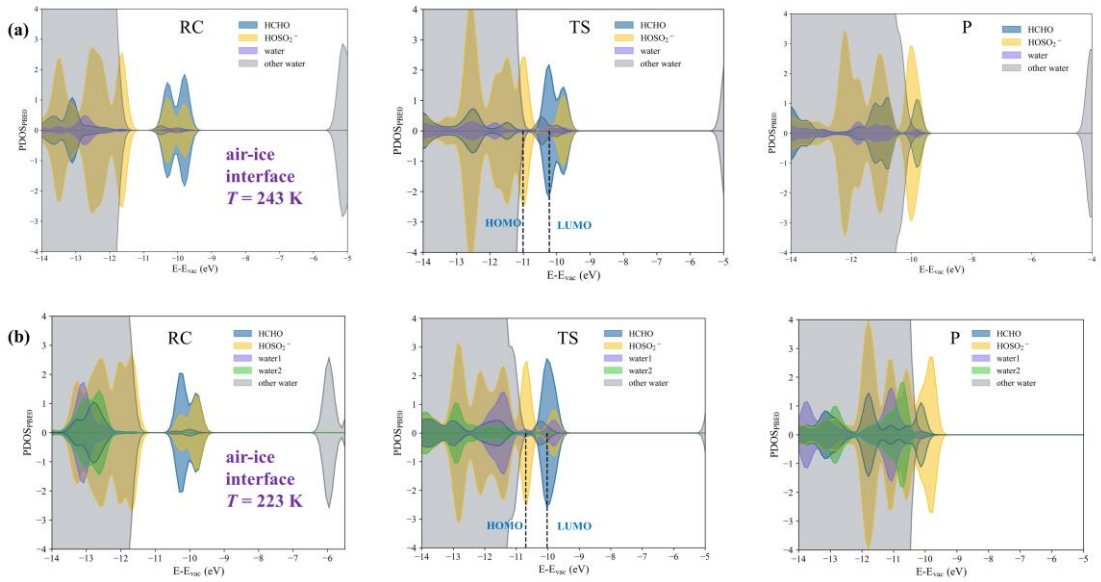


**Figure S17.** Projected density of states (PDOS) for the reactant complex (RC), transition state (TS), and product (P) along the HMS formation pathway from HCHO and $HOSO_2^-$ at the air-ice interface at (a) $T$ = 243 K, featuring a quasi-liquid layer atop crystalline ice, and (b) $T$ = 223 K, pure crystalline ice. The wavefunction calculations employed the PBE0 functional with triple-ζ basis sets and the Goedecker–Teter–Hutter (GTH) pseudopotentials. HOMO: highest occupied molecular orbital; LUMO: lowest unoccupied molecular orbital.

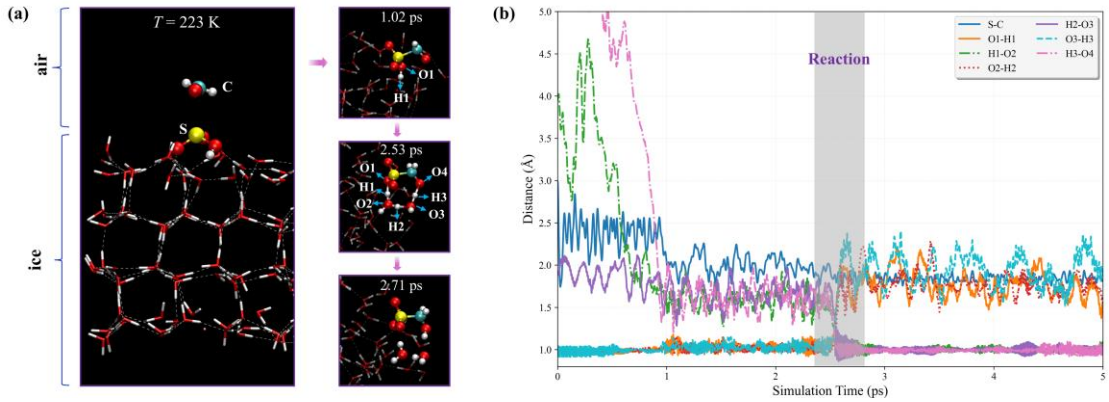


**Figure S18.** HMS formation on crystalline ice surface at $T$ = 223 K. (a) BOMD simulation snapshots showing initial configuration and reaction progression with HCHO and $HOSO_2^-$ on the ice surface. (b) Time evolution of key bond distances during the simulation.

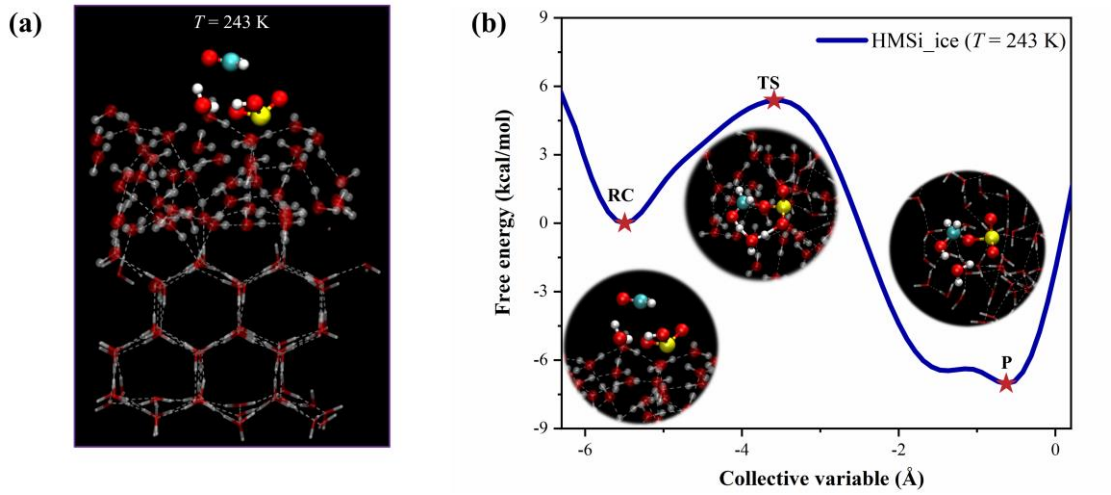


**Figure S19.** HMSi formation at the air-quasi-liquid-layer interface ($T$ = 243 K). (a) Initial metadynamics configuration showing HCHO and $HOSO_2^-$ at the interface. (b) Free energy profile along the collective variable with a 5.38 kcal/mol barrier. Insets show reactant complex (RC), transition state (TS), and product (P) structures.

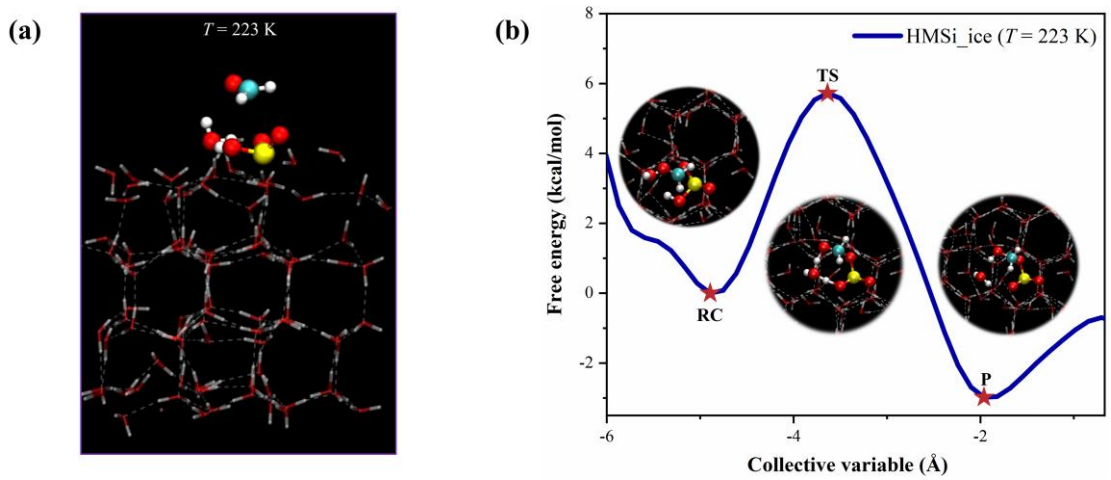


**Figure S20.** HMSi formation at the air-ice surface ($T$ = 223 K). (a) Initial metadynamics configuration showing HCHO and $HOSO_2^-$ on the crystalline ice surface. (b) Free energy profile along the collective variable with a 5.73 kcal/mol barrier. Insets show reactant complex (RC), transition state (TS), and product (P) structures.

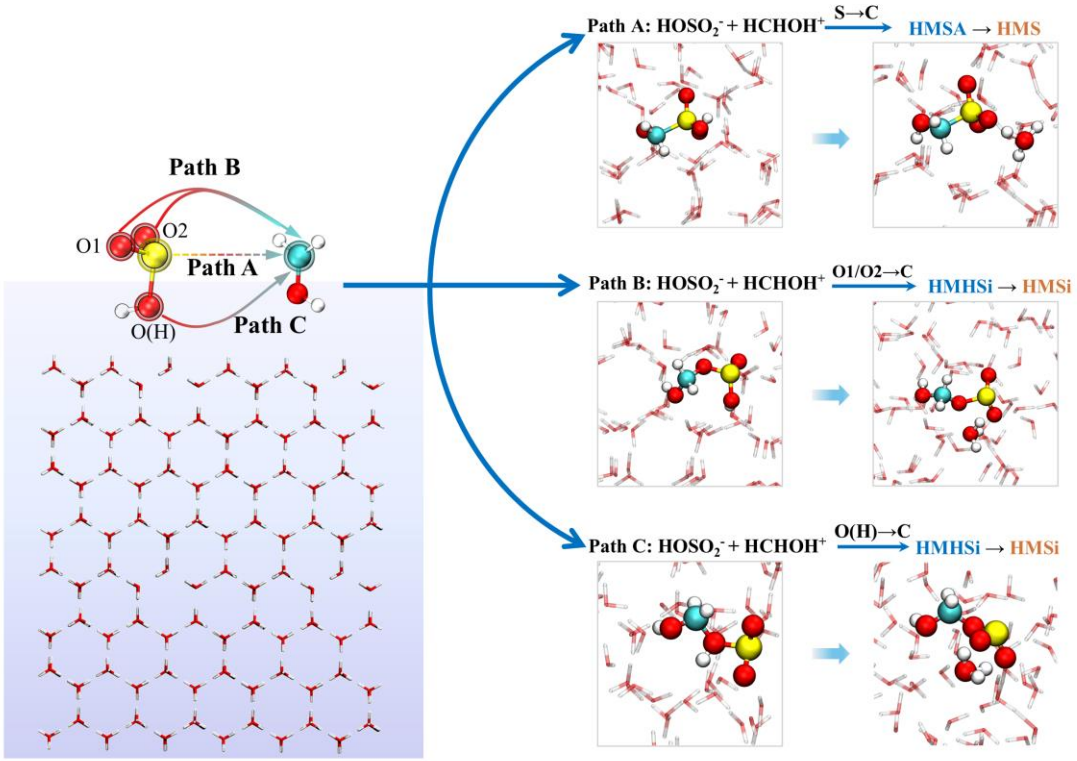


**Figure S21.** Mechanistic investigation of the reaction between $HCHOH^+$ and $HOSO_2^-$ on ice surface.

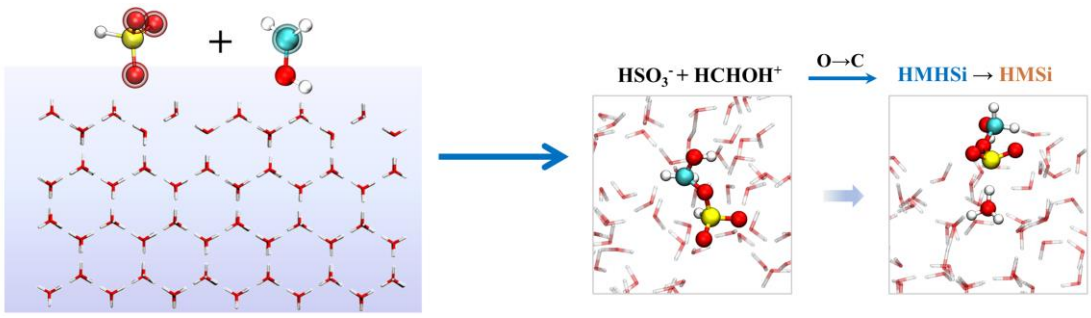


**Figure S22.** Mechanistic investigation of the reaction between $HCHOH^+$ and $HSO_3^-$ on ice surface.

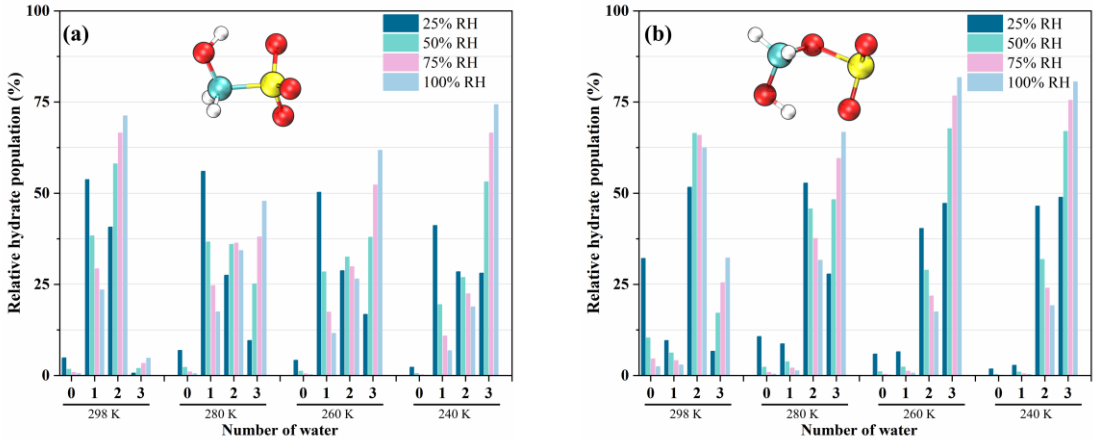


**Figure S23.** Hydration distribution (%) of (a) HMS and (b) HMSi at different relative humidity (RH = 25-100%) and temperatures ($T$ = 240-298 K).

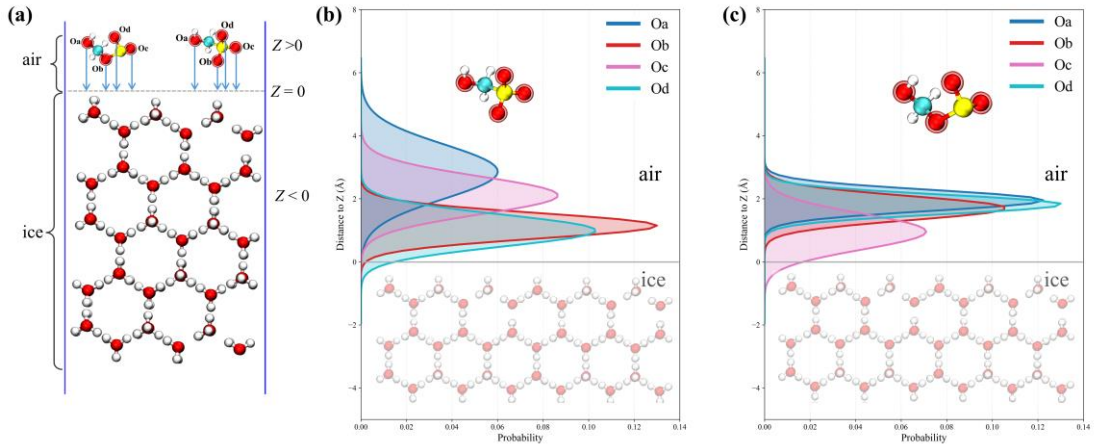


**Figure S24.** (a) Schematic representation of the ice-air interface showing the spatial arrangement of HMS/HMSi molecules with distinct oxygen atoms labeled as Oa, Ob, Oc, and Od, where Z > 0 corresponds to the air phase and Z < 0 corresponds to the ice phase. Probability distributions of distinct oxygen atoms (Oa, Ob, Oc, and Od) as a function of distance to the ice surface for HMS (b) and HMSi (c) molecules.

**References**


1. Barducci, A.; Bonomi, M.; Parrinello, M., Metadynamics. *WIREs. Comput. Mol. Sci.* **2011,** *1* (5), 826-843.
2. Barducci, A.; Bussi, G.; Parrinello, M., Well-tempered metadynamics: a smoothly converging and tunable free-energy method. *Phys. Rev. Lett.* **2008,** *100* (2), 020603.
3. Yoon, B.; Chen, S.; Voth, G. A., On the Key Influence of Amino Acid Ionic Liquid Anions on CO2 Capture. *J. Am. Chem. Soc.* **2024,** *146* (2), 1612-1618.
4. Slater, B.; Michaelides, A., Surface premelting of water ice. *Nat. Rev. Chem.* **2019,** *3* (3), 172-188.
5. Hayward, J. A.; Reimers, J. R., Unit cells for the simulation of hexagonal ice. *J. Chem. Phys.* **1997,** *106* (4), 1518-1529.
6. Martinez, L.; Andrade, R.; Birgin, E. G.; Martinez, J. M., PACKMOL: a package for building initial configurations for molecular dynamics simulations. *J. Comput. Chem.* **2009,** *30* (13), 2157-64.
7. Tang, F.; Ohto, T.; Sun, S.; Rouxel, J. R.; Imoto, S.; Backus, E. H. G.; Mukamel, S.; Bonn, M.; Nagata, Y., Molecular Structure and Modeling of Water-Air and Ice-Air Interfaces Monitored by Sum-Frequency Generation. *Chem. Rev.* **2020,** *120* (8), 3633-3667.
8. Tan, S.; Zhang, X.; Lian, Y.; Chen, X.; Yin, S.; Du, L.; Ge, M., OH Group Orientation Leads to Organosulfate Formation at the Liquid Aerosol Surface. *J. Am. Chem. Soc.* **2022,** *144* (37), 16953-16964.
9. Rappe, A. K.; Casewit, C. J.; Colwell, K. S.; Goddard, W. A.; Skiff, W. M., UFF, a full periodic table force field for molecular mechanics and molecular dynamics simulations. *J. Am. Chem. Soc.* **2002,** *114* (25), 10024-10035.
10. Zhang, J.; Dolg, M., ABCluster: the artificial bee colony algorithm for cluster global optimization. *Phys. Chem. Chem. Phys.* **2015,** *17* (37), 24173-81.
11. Stewart, J. J., Optimization of parameters for semiempirical methods VI: more modifications to the NDDO approximations and re-optimization of parameters. *J. Mol. Model.* **2013,** *19* (1), 1-32.
12. Stewart, J. J. P. *MOPAC2016*, Stewart Computational Chemistry: Colorado Springs, CO, USA, 2016.
13. Stephens, P. J.; Devlin, F. J.; Chabalowski, C. F.; Frisch, M. J., Ab Initio Calculation of Vibrational Absorption and Circular Dichroism Spectra Using Density Functional Force Fields. *J. Phys. Chem.* **2002,** *98* (45), 11623-11627.
14. McLean, A. D.; Chandler, G. S., Contracted Gaussian basis sets for molecular calculations. I. Second row atoms, Z=11–18. *J. Chem. Phys.* **1980,** *72* (10), 5639-5648.
15. Lu, T.; Chen, F., Multiwfn: a multifunctional wavefunction analyzer. *J. Comput. Chem.* **2012,** *33* (5), 580-92.
16. Mishra, H.; Enami, S.; Nielsen, R. J.; Hoffmann, M. R.; Goddard, W. A., 3rd; Colussi, A. J., Anions dramatically enhance proton transfer through aqueous interfaces. *Proc. Natl. Acad. Sci. U. S. A.* **2012,** *109* (26), 10228-32.
17. Perez, C.; Zaleski, D. P.; Seifert, N. A.; Temelso, B.; Shields, G. C.; Kisiel, Z.; Pate, B. H., Hydrogen bond cooperativity and the three-dimensional structures of water nonamers and decamers. *Angew. Chem. Int. Ed. Engl.* **2014,** *53* (52), 14368-72.
18. Lu, T.; Chen, Q., Simple, Efficient, and Universal Energy Decomposition Analysis Method Based on Dispersion-Corrected Density Functional Theory. *J. Phys. Chem. A* **2023,** *127* (33), 7023-7035.
19. Ning, A.; Li, J.; Du, L.; Yang, X.; Liu, J.; Yang, Z.; Zhong, J.; Saiz-Lopez, A.; Liu, L.; Francisco, J.

S.; Zhang, X., Heterogenous Chemistry of I2O3 as a Critical Step in Iodine Cycling. *J. Am. Chem. Soc.* **2024,** *146* (48), 33229-33238.

20. Abascal, J. L.; Sanz, E.; Garcia Fernandez, R.; Vega, C., A potential model for the study of ices and amorphous water: TIP4P/Ice. *J. Chem. Phys.* **2005,** *122* (23), 234511.

21. Kaminski, G. A.; Friesner, R. A.; Tirado-Rives, J.; Jorgensen, W. L., Evaluation and Reparametrization of the OPLS-AA Force Field for Proteins via Comparison with Accurate Quantum Chemical Calculations on Peptides. *J. Phys. Chem. B.* **2001,** *105* (28), 6474-6487.

22. Yan, J. Y.; Patey, G. N., Molecular dynamics simulations of ice nucleation by electric fields. *J. Phys. Chem. A.* **2012,** *116* (26), 7057-64.

23. Roudsari, G.; Pakarinen, O. H.; Reischl, B.; Vehkamäki, H., Atomistic and coarse-grained simulations reveal increased ice nucleation activity on silver iodide surfaces in slit and wedge geometries. *Atmos. Chem. Phys.* **2022,** *22* (15), 10099-10114.

24. Darden, T.; York, D.; Pedersen, L., Particle mesh Ewald: An N·log(N) method for Ewald sums in large systems. *J. Chem. Phys.* **1993,** *98* (12), 10089-10092.

25. Van Der Spoel, D.; Lindahl, E.; Hess, B.; Groenhof, G.; Mark, A. E.; Berendsen, H. J., GROMACS: fast, flexible, and free. *J. Comput. Chem.* **2005,** *26* (16), 1701-18.